Cloud-radiation interactions amplify ozone pollution in a warming climate

Shuyu Zhao[1], Tian Feng[2], Xuexi Tie[3], Biao Tian[4], Xiao Hu[5], Bo Hu[1], Dong Yang[1], Sinan Gu[1], Minghu Ding[4]

[1]Ningbo Meteorological Bureau, Ningbo 315012, China
[2]Department of Geography & Spatial Information Techniques, Ningbo University, Ningbo 315211, China
[3]KLACP, State Key Laboratory of Loess and Quaternary Geology, Institute of Earth Environment, Chinese Academy of Sciences, Xi'an 710061, China
[4]State Key Laboratory of Severe Weather, Chinese Academy of Meteorological Sciences, Beijing 100081, China
[5]Ningbo Zhenhai Meteorological Bureau, Ningbo 315202, China

Correspondence: Tian Feng (fengtian@nbu.edu.cn)
        Minghu Ding (dingmh@cma.gov.cn)

18   **Abstract**

19   Ozone (O_3) pollution has recently become the most critical air quality issue in China,
20   yet its underlying drivers related to climate change remain poorly understood. Here, we
21   use a regional atmospheric chemistry model, along with 10-year ground-level O_3
22   measurements, and reanalysis data on low cloud cover (LCC) and surface downward
23   shortwave radiation (SSRD) to investigate the impacts of variations in LCC, SSRD and
24   cloud-radiation interactions (CRI) on O_3 production. We design six numerical
25   experiments, and specifically modify parameters related to cloud radiation effects in
26   the chemistry module to find out the underlying cause for O_3 increase during the warm
27   season of 2022 in the Yangtze River Delta (YRD), China. Results show that O_3
28   production is strongly modulated by LCC and SSRD. The CRI plays a significant role
29   in regulating O_3 concentration, i.e., reduced LCC, increased SSRD, and a weakened
30   CRI are primarily responsible for the sharp increase in warm-season O_3 concentration
31   observed in 2022 in the YRD, China. Moreover, climate warming is likely to exacerbate
32   future O_3 pollution via weakening CRI due to fewer clouds and more SSRD. To
33   mitigate O_3 pollution, we thus propose implementing more stringent emission reduction
34   measures on O_3 precursors, along with proactive strategies to address climate change.

35

36   **Short Summary**

37   This study investigated how cloud-radiation interactions influence ozone formation in
38   a warming climate. Using measurements, reanalysis data and models, we found that
39   cloud-radiation interactions can worsen O_3 pollution and climate warming will amplify
40   the influence. We highlight that climate change will pose greater challenges for China's
41   O_3 pollution prevention and control, and actions such as reducing O_3 precursors
42   emissions and mitigating climate change are urgently needed.

43

44   **Keywords**: Ozone, cloud-radiation interactions, climate change, emission reduction
45

1 Introduction

Over the past decade, high concentrations of ground-level ozone (O_3) have increasingly been a major air pollution issue in China. These O_3 pollution events are characterized by extensive spatial coverage and prolonged duration during the warm season, i.e., from September 22 to 29, 2019, a severe O_3 pollution event in eastern China covered an area of approximately 3.2 million square kilometers (Zhang and Zheng, 2022). Another notable aspect is that high O_3 concentration often coincides with high-temperature weather, and their co-occurrence frequency has increased at a faster rate than either alone in recent years (Xiao et al., 2022), posing serious risks to human health, climate change, and food security.

Ground-level observations show that each 1°C increase results in an 8 - 10 µg m^{-3} rise in O_3 concentrations during heatwaves in eastern China, when air temperature varies between 28°C and 38°C (Pu et al., 2017; Wang et al., 2023). This is largely attributed to O_3 sensitivity to the precursors. In the VOC-limited regime, an increase in air temperature can enhance biogenic VOCs emissions, providing more O_3 precursors (Liu and Wang, 2020a). However, the response of O_3 concentration to air temperature is nonlinear. As the temperature further increases and exceeds 38.5°C, chemical and biophysical feedbacks of vegetation are suppressed, and consequently, biogenic emissions and related O_3 formation are reduced (Meehl et al., 2018; Pu et al., 2017; Steiner et al., 2010). Thus, extreme high temperature cannot fully explain high O_3 concentration. What exactly causes the highest daytime O_3 concentration in the hottest summer?

Several recent review studies have identified multiple factors to explain ground-level O_3 formation (Fu et al., 2019; Jiang et al., 2022; Lu et al., 2019a; Wang et al., 2022a), including precursor emissions and their proportion (Mousavinezhad et al., 2021; Wang et al., 2019b; Xue et al., 2014; Zeng et al., 2018; Zheng et al., 2023), climate patterns (Creilson et al., 2005; Gao et al., 2023; Hong et al., 2019; Shen and Mickley, 2017; Xu et al., 2017), synoptic-scale circulation systems (Dong et al., 2020; Ji et al., 2024; Jiang et al., 2021; Li et al., 2018; Mao et al., 2020; Shu et al., 2016; Yin et al., 2019; Zhao et al., 2010; Zhao and Wang, 2017; Zheng et al., 2023; Zhou et al., 2013), meteorological parameters such as temperature (Lu et al., 2019b; Mousavinezhad et al., 2021; Pu et al., 2017; Wang et al., 2023; Zheng et al., 2023), humidity (Mousavinezhad et al., 2021; Pu et al., 2017; Zhao and Wang, 2017; Zheng et al., 2023), wind (Mao et al., 2020; Pu et al., 2017; Zhao and Wang, 2017), and boundary layer height (Mousavinezhad et al., 2021; Zheng et al., 2023), as well as stratosphere-troposphere exchange (Lu et al., 2019a; 2019b; Verstraeten et al., 2015).

85   However, ground-level O_3 is inherently a photochemical product, and anthropogenic
86   emissions are source drivers that determine its levels, while incident solar radiation acts
87   as a trigger for photochemical reactions, dominating photolysis rates of O_3 production.
88   Currently, there are few studies on the influence of changes in solar radiation on O_3
89   formation. Early studies reported that clouds have important impacts on tropospheric
90   photochemistry, which increases global mean OH concentration by about 20% (Tie et
91   al., 2003). It was also found that the prediction accuracy of clouds in the model would
92   significantly affect atmospheric chemical composition near the surface layers, leading
93   to an overestimation/underestimation of O_3 concentration (Pour-Biazar et al., 2007).
94   During the Texas Air Quality Study II Radical and Aerosol Measurement Project, the
95   influence of clouds on photolysis rate was evidently greater than that of aerosols (Flynn
96   et al., 2010), and the total reduction in the photolysis rate caused by clouds and aerosols
97   was almost linearly correlated with the reduction in the net O_3 production. These studies
98   all indicates that changes in clouds and solar radiation significantly influence the
99   photolysis conditions, which is of great importance to O_3 formation. In China, the
100   decline in $PM_{2.5}$ concentration is considered one of the reasons for the increase in O_3
101   levels in recent years due to the weakened aerosol-radiation interactions (Yang et al.,
102   2022). However, there are lack of field campaign evidences similar to those of the USA
103   (Flynn et al., 2010), and only in recent years, fewer studies have qualitatively described
104   the influence of solar radiation on O_3 concentration. For example, enhanced solar
105   radiation during hot and dry weather can increase O_3 production (Mousavinezhad et al.,
106   2021; Xia et al., 2022; Yin et al., 2019; Zhao and Wang, 2017). Some of these studies
107   have also mentioned that cloud cover can alter solar radiation, thereby affecting O_3
108   formation (Xia et al., 2022; Zhao and Wang, 2017). Nonetheless, these studies are lack
109   of quantitative analysis and systematic mechanism explanations of the contributions of
110   clouds, solar radiation, and their variability to O_3 formation, and none of them further
111   investigate the impact of cloud-radiation interactions (CRI) on O_3 formation. Moreover,
112   with an increasingly persistent impact of climate change, how this factor may affect O_3
113   concentration remains unclear.

114   In this study, we establish correlations between daytime O_3 concentration and
115   downward solar radiation as well as low clouds, based on measurements and reanalysis
116   data during the past decade. Using numerical models, we analyze the causes of high O_3
117   concentration and, in particular, assess the dependence of O_3 change on the variabilities
118   of clouds, solar radiation and CRI. Furthermore, we project the potential impacts of
119   these factors on high O_3 concentration under climate change.

120
121   **2   Data and Methods**
122   **2.1 Measurements and reanalysis data**
123   We collect *in-situ* measurements on hourly mass concentrations of gaseous pollutants
124   in the Yangtze River Delta (YRD), China during the warm season of the past decade

125 (2014-2024). The gaseous pollutants include O_3, CO and NO_2, which are measured by
126 Model 49i UV Photometric Ozone (O_3) Analyzer, Model 48i Gas Filter Correlation
127 Carbon Monoxide (CO) Analyzer, and Model 42i Chemiluminescence $NO-NO_2-NO_x$
128 Analyzer, respectively. These analyzers are equipped with built-in calibration systems
129 that accurately linearize the instrument outputs. The missing data have been eliminated.
130 The flat YRD region, located in eastern China, is one of the largest urban
131 agglomerations in the world, consisting of three provinces (Jiangsu, Zhejiang, and
132 Anhui) and one municipality (Shanghai) (Fig. 1a). This region is densely populated,
133 with highly developed economies and transportation networks, and concurrently,
134 anthropogenic emissions of O_3 precursors, including nitrogen oxides (NO_x) and volatile
135 organic compounds (VOCs) are significantly higher than those in other regions of
136 China (Figs. 1b and 1c). Moreover, the region has abundant vegetation, resulting in a
137 moderate level of biogenic VOCs emission in China (Fig. 1d). Thus, this region is one
138 of China's hotspots for O_3 pollution. The warm season in mid-latitude regions of
139 Northern Hemisphere often refers to the April -September period. In these six
140 consecutive months within a single calendar year, the highest mean O_3 concentration is
141 observed, defined as the warm-season O_3. The YRD belongs to the mid-latitude region
142 (Fig. 1a), and is facing an environment issue of high O_3 concentration during the warm
143 season.
144
145 Meteorological reanalysis data used here consist of surface downward shortwave
146 radiation (SSRD) and low cloud cover (LCC) from the European Centre for Medium-
147 Range Weather Forecasts ERA5, with an hourly resolution and a $0.25° \times 0.25°$ spatial
148 resolution. SSRD and LCC data are selected from 07:00 to 18:00 Beijing Time (BJT)
149 due to O_3 photochemical formation occurred during the daytime. Hourly observations
150 on 2-m temperature (T2m), relative humidity (RH), wind speed (WS) and direction
151 (WD) observed at four weather stations are from the National Oceanic and Atmospheric
152 Administration, available on the website of https://www.ncei.noaa.gov/maps/hourly/.
153
154 **2.2 Model and experiments**
155 We use a state-of-the-art regional Weather Research and Forecasting Model online
156 coupled with chemistry (WRF-Chem model) to investigate the causes of high O_3
157 concentration during the warm season of 2022. The WRF-Chem model is a regional
158 atmospheric chemistry transport model that can assess how the physical and chemical
159 processes including transport, vertical mixing, aerosol-cloud interactions, cloud-
160 radiation interactions, emissions, and gas-to-particle conversion affects air quality. The
161 detailed model information refers to Grell et al. (2005), and model configurations used
162 in this study are as follows. The physical mechanisms include the Goddard longwave
163 and shortwave radiation schemes (Dudhia, 1989), the WSM 6-class graupel
164 microphysics scheme (Hong and Lim, 2006), the Mellor-Yamada-Janji (MYJ)

165 planetary boundary layer scheme (Janjić, 2002), the unified Noah land-surface model
166 (Chen and Dudhia, 2001) and Monin-Obukhov surface layer scheme (Janjić, 2002).
167 The chemical mechanisms include a new flexible gas-phase chemical module and the
168 Community Multiscale Air Quality (CMAQ, version 4.6) aerosol module developed by
169 the United States Environmental Protection Agency (U.S. EPA) (Binkowski, 2003),
170 gas-phase reactions of volatile organic compounds (VOCs) and nitrogen oxide (NO_x)
171 by the SAPRC-99 (Statewide Air Pollution Research Center, version 1999), and a non-
172 traditional volatility basis-set (VBS) approach to calculate secondary organic aerosol
173 (SOA) formation (Li et al., 2011b). In addition, HONO production by NO_2
174 heterogeneous reaction is added to improve HO_x ($OH+HO_2$), NO_x, O_3, and SOA
175 simulations (Li et al., 2010). Inorganic aerosols use the ISORROPIA mechanism
176 (version 1.7) (Nenes et al., 1998), in which a SO_2 heterogeneous reaction to sulfate
177 formation on aerosol surfaces is considered (Li et al., 2017a). A fast Tropospheric
178 Ultraviolet and Visible (FTUV) radiation transfer model is used to calculate the
179 photolysis rates (Tie et al., 2003), which can also calculate the impacts of aerosols and
180 clouds on the photochemistry processes (Li et al., 2011a). The wet deposition uses the
181 method in CMAQ (Byun and Ching, 1999) and the dry deposition follows Wesely
182 (1989). Anthropogenic emission inventory uses the Multi-resolution Emission
183 Inventory for China (MEIC) developed by the Tsinghua University (Li et al., 2017b),
184 consisting of industrial, power, transportation, agricultural, and residential sources. The
185 biogenic emissions are calculated by the Model of Emissions of Gases and Aerosol
186 from Nature (MEGAN) (Guenther et al., 2006). The model horizontal resolution is 6
187 km, with 200 grids in the longitude and 200 grids in the latitude. There are 35 vertical
188 sigma levels, with intervals ranging from 50 m near the surface to 500 m at 2.5 km
189 above the ground level, and more than 1 km above 14 km. Initial and boundary
190 meteorological fields in the model are driven by 6-hour 1° × 1°Final Analyses data from
191 National Centers for Environmental Prediction (NCEP FNL). Chemical initial and
192 boundary fields are from a Community Atmosphere Model with chemistry (CAM-
193 Chem) 6-hour output. The spin-up time of the model is 2 days. A brief introduction on
194 the schemes used in this study is shown in Table S1.
195
196 We perform four groups of model experiments, with a total of six simulations (Table
197 1). The baseline experiment (BS_Exp.) reflects the real situation of high O_3
198 concentration. The BS_Exp. uses real emissions and meteorological conditions in July,
199 2022. The rationality for selecting July as the representative month of the warm season
200 is as follows. Firstly, July is typically the most representative month for the warm
201 season in Northern Hemisphere. Moreover, the observed interannual variation in
202 daytime O_3 concentration in July is fully consistent with the interannual variation in
203 warm-season mean O_3 concentration in recent years (Figs. S1 and 2a). Most importantly,
204 daytime O_3 concentration in July 2022 is the highest in recent years, significantly higher

205 than the lowest in July 2021, and another identical feature is that daytime O_3
206 concentration in July 2024 is the second highest. The BS_Exp. is also used to validate
207 the model performance by comparing with the measurements. Another two groups of
208 control experiments (CTRL_Exp.) are used to assess the impacts of interannual
209 variability of meteorology and emission change on O_3 formation. The first group of
210 control experiments selects the year of 2021 with the lowest daytime O_3 concentration
211 in recent 5 years, using the same emissions as the BS_Exp. but different meteorological
212 conditions (defined as CTRL_Exp.1). Differences between the CTRL_Exp.1 and
213 BS_Exp. can illustrate the impacts of interannual variability of meteorological
214 conditions on O_3 concentration. The second group uses the same meteorological
215 conditions as the BS_Exp. but different emissions (CTRL_Exp.2). Emission changes
216 in CTRL_Exp.2 are based on the emissions in 2021, and the difference between
217 CTRL_Exp.2 and the BS_Exp. can explain the impact of emission changes of
218 precursors on O_3 formation. In addition, we perform a background experiment
219 (BG_Exp.) with zero anthropogenic emissions to calculate the background O_3
220 concentration.

221

222 Based upon the BS_Exp. and CTRL_Exp.1, we particularly examine the contribution
223 of CRI intensity to O_3 formation *via* considering and not considering the impact of CRI
224 on atmospheric photochemistry. The BS_Exp. experiments with CRI considered or not
225 are designated as BS_Exp._CRI and BS_Exp._noCRI, respectively, while the
226 CTRL_Exp.1 experiments with and without CRI are designated as CTRL_Exp.1_CRI
227 and CTRL_Exp.1_noCRI. The setup information for all simulation experiments is
228 provided in Table 1. The impacts of clouds on solar radiation are calculated by adjusting
229 three key parameters in the chemical module related to cloud radiative effect: cloud
230 optical depth, single scattering albedo, and asymmetry factor. This approach confines
231 the CRI impact within photochemical reactions, only altering the photolysis rates of
232 photochemical substances directly associated with O_3 formation. Additionally, it avoids
233 the original meteorological fields in the physical module being perturbed by the CRI,
234 which would otherwise complicate the study.

235

236 To evaluate the model performance, we use three common statistical indices involving
237 mean bias (MB), root mean square error (RMSE), and index of agreement (IOA)
238 (Willmott, 1981). The formulas are as follows:

239
$$MB = \frac{1}{N}\sum_{i=1}^{N}(P_i - O_i) \qquad (1)$$

240
$$RMSE = \left[\frac{1}{N}\sum_{i=1}^{N}(P_i - O_i)^2\right]^{\frac{1}{2}} \qquad (2)$$

241
$$IOA = 1 - \frac{\sum_{i=1}^{N}(P_i - O_i)^2}{\sum_{i=1}^{N}(|P_i - \overline{O}| + |O_i - \overline{O}|)^2} \qquad (3)$$

242   where P_i and O_i represented the simulated and observed variables, respectively. N is the
243   total sample number of the simulation, and $\bar{O}$ denotes the average of the observation.
244   The IOA ranges from 0 to 1. The closer it is to 1, the better the simulation.
245
246   **2.3 Climate Scenarios**
247   Using 41-model results from Coupled Model Intercomparison Project Phase 6 (CMIP6)
248   (Table S2), we analyze the long-term trends of monthly surface downwelling shortwave
249   radiation (SSRD), total cloud cover percentage (TCC), and daily maximum air
250   temperature (T_max) in July during 2025-2099 under three Shared Socio-economic
251   Pathways (SSPs). These three SSPs narrate the Green Road with a sustainable
252   development paradigm (SSP1-1.9), middle-of-the road along a historical development
253   pattern (SSP2-4.5), and a highway road with a fossil-fueled development pattern
254   (SSP5-8.5) that represent high, moderate, and low climate mitigation pathways,
255   respectively (Riahi et al., 2017). Finally, we project the potential influence of the solar
256   radiation on the occurrence of high O_3 concentration under these climate scenarios.
257
258   **3 Results and discussion**
259   **3.1 Observed linkage between O_3, incident solar radiation, and low clouds**
260   Over the past decade, the warm-season mean daytime O_3 concentration (hereafter O_3
261   concentration) in the YRD has shown a distinct rising-falling pattern before 2021, with
262   a turning point in 2017 (Fig. 2a). From 2013 to 2017, O_3 concentration increased by 5.9
263     $\mu g\ m^{-3}$ per year, while decreased by 2.5 $\mu g\ m^{-3}$ per year during 2017-2021. Due to the
264   Action Plan on Prevention and Control of Air Pollution since 2013, China's
265   anthropogenic NO_x emissions were substantially reduced (Zhang et al., 2019), whereas
266   VOCs emissions increased slightly during 2013-2017 (Zheng et al., 2018). The
267   disproportionate emission reductions largely contributed to the continuous increase in
268   O_3 concentration from 2013 to 2017 (Jiang et al., 2022; Wang et al., 2022a; Liu and
269   Wang, 2020b; Wang et al., 2019a). Since 2017, as VOCs emissions began to decline
270   (Jiang et al., 2022; Simayi et al., 2022), along with the ongoing reduction in NO_x (Li et
271   al., 2024; Zhang et al., 2019), O_3 concentration began to decline (Lu et al., 2019b). In
272   addition to precursor emissions, O_3 trends during this period were also influenced by
273   meteorological conditions and $PM_{2.5}$ reductions. The meteorological conditions play an
274   important but not dominant role in ozone trends (Liu et al., 2023; Li et al., 2020), and
275   the continued $PM_{2.5}$ reduction enhances ozone production due to the weakened aerosol
276   uptake of hydroperoxyl (HO_2) radicals (Li et al., 2019a). Nevertheless, O_3 trends was
277   primarily driven by changes in precursor emissions (Wang et al., 2022a; Liu and Wang,
278   2020b). Unexpectedly, during the warm season of 2022, O_3 concentration suddenly
279   increased to the highest, even surpassing the turning point of 2017 by 3.4 $\mu g\ m^{-3}$.
280   Subsequently, O_3 concentrations dropped during the warm seasons of 2023-2024

281   compared to the same period of 2022, but still remained at relatively high levels. This
282   is seemingly paradoxical to emission reductions in O_3 precursors mentioned above.

283

284   According to the principle of O_3 formation, it is influenced not only by changes in
285   precursor emissions but also by the solar radiation intensity. Observational evidence
286   reveals that interannual variability of warm-season downward solar radiation is highly
287   consistent with the interannual variation of O_3 concentration in the YRD during the past
288   decade. A significant positive correlation between them (*r = 0.85, p < 0.001*, Fig. 2b)
289   suggests that O_3 concentration indeed strongly depends on the SSRD intensity. Low
290   clouds with small and compact liquid droplets can significantly reflect the solar
291   radiation by their considerable optical thickness (Kang et al., 2020), thereby
292   diminishing photolysis rate and the loadings of tropospheric oxidants (Tie et al., 2003;
293   2019). We examined the relationship between daytime LCC and O_3 concentration, and
294   found that O_3 concentration is more significantly negative with LCC (*r = -0.90, p <*
295   *0.001*, Fig. 2c). This suggests that low clouds are of great importance to O_3
296   concentration. Liu and Wang (2020a) suggested that the reduction of cloud cover plays
297   a dominant role in increasing daily maximum 8-hour (MDA8) O_3 concentration in
298   China during 2014-2017 summer. Similarly, daytime LCC in the warm season of 2022
299   dropped to the lowest (LCC = 0.2) during the past decade, with a 23.6% reduction
300   relative to the multi-year mean, while SSRD was significantly more than the multi-year
301   mean by 28.9 W m^{-2} (Fig. S2). Thus, solar radiation is vital to O_3 formation, by which
302   an increase (decrease) in LCC intensifies (weakens) the reflection of solar radiation,
303   and decreases (increases) SSRD, inconducive (conducive) to O_3 formation. The
304   favorable solar radiation is likely crucial to the sudden increase in O_3 concentration
305   during the warm season of 2022, though O_3 precursors from anthropogenic emissions
306   have been slashed.

307

308   **3.2 Model validation**

309

310   Observations at weather stations in four provinces and municipality are used to validate
311   the model performance on meteorological fields. Results show that the model well
312   captures spatiotemporal variability of meteorological parameters (Fig. S3). For
313   example, the simulated T2m is in good agreement with the observation, with the IOAs
314   in the range of 0.88-0.92. The MBs are within 0.7°C, and the RMSEs are around 2.0°C.
315   Followed by the RH, with IOAs of 0.83 to 0.89. Most importantly, the model
316   successfully captures the WD shift, with the IOAs of 0.79 to 0.89, which is crucial for
317   accurately simulating atmospheric transport and re-distribution of the spatiotemporal
318   variations in pollutants. There are also some biases between the simulations and
319   observations. The model generally overestimates the WS, with the IOAs between 0.60
320   and 0.73, lower than those of the three parameters mentioned above. These

321   discrepancies are partly due to the systematical bias of the WRF-Chem model, which

322   often overestimates the ground-level WS. Additionally, the observation data on WS are

323   recorded only as integers, with no decimal fractions. This lack of precision in

324   observations reduces the temporal variability of the WS, compared to the simulations,

325   thereby resulting in a lower IOA.

326

327   For pollutants, the model also well reproduces temporal variation of O_3, with an MB of

328   2.4 $\mu g\ m^{-3}$ and an RMSE of 17.7 $\mu g\ m^{-3}$ (Fig. S4a). This means the simulation is

329   approximately 2.8% higher than the observation, with an accuracy of 79.3%. The IOA

330   between the simulated O_3 hourly variation and the observation exceeds 0.90 (IOA =

331   0.94), implying for a better performance of the model on chemical reactions. The

332   simulated NO_2 concentration is also in a good agreement with the observation (IOA =

333   0.83), with an MB of 0.9 $\mu g\ m^{-3}$ and an RMSE of 5.3 $\mu g\ m^{-3}$ (Fig. S4b). Inevitably there

334   are also some discrepancies between the simulation and the observation, i.e, the

335   amplitude of the simulated CO concentration is remarkably greater than the observed

336   (Fig. S4c). This is largely related to the emission inventory that fails to depict an

337   accurate diurnal cycle of CO emission. The IOA between the simulated and observed

338   CO concentrations is thus relatively lower (IOA = 0.63). However, the simulated mean

339   CO concentration is extremely close to the observation (MB = 0.0 $\mu g\ m^{-3}$), suggesting

340   that the model accurately captures the variability of atmospheric transport. Generally,

341   the model well reproduces temporal variations in meteorological fields, O_3 and related

342   gaseous pollutants (Figs. S3-S4), providing sufficient evidence on the rationality of the

343   model.

344

345   **3.3 Modelling evidence on O_3 increase**

346   To verify this hypothesis, we separately distinguished contributions of background

347   fields, anthropogenic emissions and their changes, as well as changes in meteorological

348   fields to O_3 concentration. Meteorological and chemical lateral boundary inputs, and

349   biogenic emissions approximately produce 57.7 $\mu g\ m^{-3}$ of O_3 concentration in the YRD

350   in the warm season of 2022, accounting for 55.1% of O_3 concentration (Fig. 3). Another

351   study also found that background inputs contributes 39 to 58 $\mu g\ m^{-3}$ to summertime

352   MDA8 O_3 concentration in this region (Li et al., 2019b). These results reveal a

353   relatively high level of background O_3 concentration in the YRD, which provides a

354   favorable environmental basis for the occurrence of O_3 pollution. When anthropogenic

355   emissions are included, O_3 concentration increases by 47.1 $\mu g\ m^{-3}$, suggesting that

356   human emissions remain a key contributor to O_3 formation.

357

358   We further investigated the impact of changes in anthropogenic emissions on O_3

359   concentration. Based upon the interannual variations in anthropogenic emissions, NO_x

360   and VOCs emissions in the summer of 2022 are approximately reduced by 5% and 4%,

361   respectively, compared to the summer of 2021 (Jiang et al., 2022; Li et al., 2024).

362   Consequently, O_3 concentration decreased by 1.5 µg m^{-3} (Fig. 3), meaning that current

363   emission reductions definitely lead to a decline in O_3 concentration. As summertime O_3

364   sensitivity changes from a VOC-limited regime to a transitional regime in the YRD

365   (Wang et al., 2019a; 2022b; Yin et al., 2019), simultaneous reductions in VOCs and

366   NO_x emissions have become an effective way to reduce O_3 concentration. Nonetheless,

367   the O_3 drop through emission cuts is not as significant as expected. Therefore, the

368   changes in anthropogenic emissions are not responsible for the increase in O_3

369   concentration in the warm season of 2022, and more stringent measures on emission

370   reductions are needed to achieve a desired O_3 decline.

371

372   Besides the impacts of human emissions, we examined the influence of meteorology

373   change, because the change is of great significance to the trend of O_3 concentration,

374   even exceeding the impact of changes in anthropogenic emissions (Liu and Wang,

375   2020a). As a result, differences in meteorological fields alone lead to a 9.2 µg m^{-3}

376   increase of O_3 concentration in July 2022 relative to the same period of 2021 (Fig.3).

377   This is roughly consistent with Ji et al. (2024), who suggested adjustments of

378   meteorological fields lead to an increase in O_3 concentration by 13.0 µg m^{-3} in coastal

379   cities of the YRD in July 2022 compared to 2015-2021. Thus, meteorological

380   conditions in the warm season of 2022 are more favorable for O_3 formation in the YRD.

381   Noticeably, the negative effects of interannual variability of meteorological conditions

382   on O_3 concentration have greatly exceeded the positive effects of precursor emission

383   reductions.

384

385   Furthermore, we specifically assessed the impacts of shortwave solar radiation, low

386   clouds, and CRI on O_3 concentration, because the solar radiation is the direct

387   meteorological factor for O_3 formation. The model also well reproduces the interannual

388   variability of LCC and SSRD, i.e., the calculated changes in LCC and SSRD are 0.07

389   and 83.5 W m^{-2}, respectively, close to the observed 0.09 and 82.7 W m^{-2} (Fig. S5).

390   These comparisons mean that the calculated interannual variability of LCC is

391   approximately 22.2% lower than the observations, while SSRD variability is

392   overestimated by about 1.0%. This may lead to a little underestimation of the impact of

393   LCC and SSRD variabilities on O_3 formation. Generally, the model evidence confirms

394   the observed linkage that an increase (decrease) in LCC and a decrease (increase) in

395   SSRD can suppress (enhance) O_3 production (Fig. S6). As LCC increase, the SSRD

396   reduces significantly at a rate of more than 40 W m^{-2} per 0.1 increase in LCC (Fig. S6a).

397   In particular, the SSRD decreases more rapidly in the early stage when low clouds

398   appear. As a result, the photolysis rate rapidly drops and O_3 production significantly

399   slows down. As LCC further increases, daily mean SSRD falls below 400 W m^{-2},

400   resulting in a noticeable slowdown in photolysis rates, falling to less than 4.0×10^{-3} s^{-1}

401 (Fig. S6b). Consequently, the rate of O_3 production slows, and O_3 concentrations are
402 not as high as that occurred in the early stage (Fig. S6c). Noticeably, the correlation
403 between O_3 concentration and SSRD is less more significant than the correlations in
404 Figs. S6a and S6b, with a confidence level exceeding 95% (whereas the first two panels
405 show confidence levels exceeding 99.9%). The data are also distributed more
406 dispersedly. This is largely due to solar radiation is one key factor influencing O_3
407 production. Precursors emissions and their proportion are the other key factor. In
408 addition, O_3 concentration is also affected by atmospheric transport, deposition, and
409 stratosphere-troposphere exchange mentioned in *Section Introduction*.
410
411 Unfortunately, current models are unable to fully isolate the individual contribution of
412 variability in LCC and SSRD to O_3 production. As a compromise, we managed to
413 examine the response of O_3 concentration to the CRI. In July 2022, clear-sky weather
414 dominates in the YRD, with monthly mean daytime LCC noticeably lower than that in
415 2021 (Figs. 4a and 4b). The regional average daytime LCC and SSRD are 0.04 and
416 583.20 W m^{-2}, respectively (Figs. 4a and 4c). Compared to July 2021 (Figs. 4b and 4d),
417 LCC decreases by 63.6%, while SSRD increases by 16.7%. This clear and cloudless
418 weather favors O_3 formation. Consequently, the magnitude and spatial coverage of high
419 O_3 concentration are significantly larger (Figs. 4e and 4f). Less LCC in July 2022
420 reflects less incident solar radiation, resulting in less attenuation to incident solar
421 radiation and more solar radiation reaching the surface. This minimal impact of clouds
422 on incident solar radiation is defined as a weak CRI. By comparison, more LCC in July
423 2021 enhances the reflection of incident solar radiation, and consequently, less incident
424 solar radiation reaches the surface, leading to a strong CRI. Whether the CRI is strong
425 or weak, it reduces SSRD and decelerates the photolysis rate, thereby suppressing
426 ground-level O_3 production (Figs. 5a, 5b, and S6). The stronger (weaker) the CRI, the
427 more (less) the O_3 reduction. The change in O_3 concentration (ΔO_3) is highly sensitive
428 to the LCC when low clouds are fewer (Fig. S6). A little increase in LCC can cause a
429 sharp decline in O_3 production, resulting in a significant reduction in O_3 concentration.
430 For example, when LCC is less than 0.3, an increase of 0.1 in LCC approximately leads
431 to a reduction of 3.5 µg m^{-3} in ΔO_3. When LCC is more than 0.3, the photolysis rates
432 decrease to a lower level (Figs. S6a and S6b), and ΔO_3 drops not as rapidly as that in
433 the initial stage of clouds occurrence, with a decline rate of 2.4 µg m^{-3} for an additional
434 0.1 increase in LCC (Fig. S7). Such changes in LCC and SSRD can lead to variations
435 in the CRI, resulting in significantly different impacts on O_3 production. Compared
436 with the summer of 2021, the weaker CRI in the summer of 2022 leads to a widespread
437 and substantial increase in O_3 change over the YRD, with the maximum increase
438 exceeding 9 µg m^{-3} on a local scale (Fig. 5c). This implies that a weakened CRI
439 suppresses O_3 formation less effectively, thereby indirectly enhancing O_3 production,
440 with a regional mean O_3 increase of 2.9 µg m^{-3} (Fig. S8).

441

442   Based on the above results, contributions of different factors to O_3 increase over the

443   YRD in the summer of 2022 are shown in Fig. S8. Changes in meteorological

444   conditions including the reduction in LCC and the increase in SSRD lead to an increase

445   of 9.2 $\mu g\,m^{-3}$ in O_3 concentration. Thereinto, the weakened CRI due to the reduced LCC

446   and increased SSRD contributes to 2.9 $\mu g\,m^{-3}$, accounting for 31.5% of the total O_3

447   increase caused by favorable meteorological conditions. In contrast, anthropogenic

448   VOCs and NO_x emission reductions lead to a decrease of 1.5 $\mu g\,m^{-3}$ in O_3 concentration,

449   which is far less than the impact of the changes in photolysis conditions. This indicates

450   that the reduction in LCC, the increase in SSRD, and the weakened CRI are the major

451   drivers of the sudden increase in O_3 concentration over the YRD during the summer of

452   2022.

453

454   **3.4 O_3 pollution potential under global warming**

455   We used CMIP6 products to analyze the long-term trends of T_{max}, SSRD, and TCC

456   under SSP5-8.5, SSP2-4.5 and SSP1-1.9 (Fig. 6). The projected climate change under

457   each SSP deviates significantly from the ERA5 reanalysis data, particularly in terms of

458   the interannual variability, which is remarkably larger in reality. This indicates that

459   climate change is highly uncertain. Nevertheless, the projected trend of T_max is

460   generally consistent with the ERA5. The TCC pattern also align well with the SSP2-

461   4.5 projection in recent years, and the SSRD pattern also closely matches the SSP2-4.5

462   projection. This consistency roughly corresponds with the development pathway in

463   China over the past decade. These comparisons suggest that the projections under

464   different SSPs provide valuable information on understanding future climate change

465   and its implications for O_3 pollution.

466

467   Ensemble mean T_{max} will continue to rise during the 21st century under any SSPs,

468   whether the extreme or mean T_{max} (Figs. 6a and 6b). Noticeably, until the end of the

469   21st century, T_{max} extreme no longer increases significantly and exhibits a fluctuation

470   pattern under SSP1-1.9. However, under the two alternative scenarios, the T_{max} will

471   continuously increase more significantly, with an annual mean rate of 0.3°C per decade

472   (Figs. 6a and 6b). While under SSP5-8.5, the temperature will follow a linear increase

473   trend at a faster rate that is more than twice as that under SSP2-4.5. Although there are

474   some differences in the warming rates by models and scenarios, the warming trend is

475   highly consistent.

476

477   Observational evidence shows that climate warming has increased the frequency of

478   high temperatures and O_3 extremes (Wang et al., 2023). Consequently, the frequency

479   of extreme high-temperature events coinciding with high O_3 concentrations, as

480   observed in 2022, may also increase (Hong et al., 2019; Xiao et al., 2022). Heatwaves

481 are often accompanied by adiabatic subsidence, fewer clouds, and stronger solar
482 radiation. Cloud cover shows no significant trend under SSP1-1.9, whereas it decreases
483 significantly under SSP2-4.5 and SSP5-8.5, with a faster decline rate under SSP5-8.5
484 (Fig. 6c). Concurrently, SSRD exhibits a significantly increasing trend under three
485 SSPs (Fig. 6d). Though in the second half of the 21st century, SSRD fluctuates within
486 a smaller magnitude under SSP1-1.9, it is still higher than that in the first half of the
487 21st century. Under SSP2-4.5 and SSP5-8.5, SSRD increases more rapidly at almost the
488 same rate (Fig. 6d).

490 There are some differences in the trends of radiation factors related to O_3 formation
491 under different scenarios inevitably. For example, the phases of SSRD and clouds under
492 SSP1-1.9 significantly differ from those under the other two scenarios. However, all
493 scenarios are highly favorable for an increase in SSRD, suggesting that the potential
494 risk of high O_3 concentrations may be increasing in the forthcoming decades, even
495 taking the Green Road. Fortunately, based on recent emission inventories, pollutants in
496 China have shown a decreasing trend. In our study, by comparison with emissions in
497 the summer of 2021, VOCs and NO_x emissions in the summer of 2022 decreased by 4%
498 and 5%, respectively (Jiang et al., 2022; Li et al., 2024), leading to a reduction in O_3
499 concentration by 1.5 µg m^{-3}. According to these emission reduction rates, we use a
500 simple linear extrapolation method, also in conjunction with China's carbon neutrality
501 goal, to estimate VOCs and NO_x emissions in the future. By the 2030 carbon peak,
502 VOCs and NO_x emissions will have been reduced by approximately 31% and 37%,
503 respectively, relative to 2021 levels. By the 2060 carbon neutrality goal, the reductions
504 are projected to reach 80% and 87%, respectively. Actually, emission reductions may
505 face challenges and unlikely to follow such a perfect pathway, and the response of O_3
506 concentration to precursor reductions is also nonlinear. We thus assume that, if such an
507 idealized scenario is followed, O_3 concentrations by 2030 and 2060 are estimated to be
508 reduced by 13.5 µg m^{-3} and 58.5 µg m^{-3}, respectively, relative to the levels in 2021.
509 Therefore, in the long term, on the decadal scale, the continued emission reductions are
510 expected to significantly reduce O_3 concentration.

512 However, on an interannual scale, the projected SSRD variability can reach several tens
513 of W m^{-2}, which is consistent with this study. Our study shows that interannual
514 difference in SSRD between the summers of 2022 and 2021 is more than 80 W m^{-2}.
515 Based on the linear relationship between O_3 and SSRD shown in Fig. 2, such
516 differences in SSRD corresponds to a change of 28 µg m^{-3} in daytime O_3 concentration.
517 According to the spatial distribution in Fig. 4, the regional mean daytime O_3 change
518 due to meteorological changes (including clouds and SSRD) is 9.2 µg m^{-3}. Thus, a
519 sudden increase in SSRD may partially offset the benefits of emission reductions. Given
520 that coordinated VOCs and NO_x emission reductions are in the early stage, the

increasing possibility of highly favorable photochemical conditions under climate change could not only counteract the effects of emission reductions, but may even lead to a rebound in O_3 concentrations in the short term. Moreover, less clouds and more SSRD under SSPs will also weaken CRI and consequently aggravate O_3 pollution in the future. Based on SSPs projections, the interannual differences of summer SSRD and cloud cover could reach or even exceed those observed between the summers of 2022 and 2021 (the interannual differences in SSRD and LCC is 82.7 W m^{-2} and 0.09, respectively). It is reasonable to expect that the CRI interannual variability will likely exert an influence on O_3 changes that is no less significant than the calculation presented in this study. Though these factors related to climate change are highly variable, based upon the past and present impacts on O_3 concentration, their impacts on future O_3 pollution control are widely believable. Thus, we suggest that, if anthropogenic emission reductions are insufficient, these changes in clouds and SSRD linked to climate change will increase O_3 concentration during the warm season.

4 Conclusions and implications

High O_3 concentration during the warm season have been increasingly becoming a major air pollution issue in China, however, whether it is closely connected to climate change has not yet received sufficient attention. Our findings indicate that the sudden increase in O_3 concentration in the YRD during the warm season of 2022 is closely linked to the weak CRI characterized by lower LCC and higher SSRD. Less LCC favors more solar shortwave radiation reaching the surface, which significantly accelerates photochemistry, thereby leading to a pronounced increase in O_3 concentration.

The notable increase in O_3 concentration caused by weakened CRI has significantly exceeded the O_3 reduction caused by the interannual decrease in precursor emissions during the warm season of 2022, attenuating the benefits of precursor emission reductions. We emphasize that the focus on LCC and SSRD is with significant implications for operational forecast on O_3 pollution, i.e., more stringent measures on precursor emission reductions are imperative under weaker CRI.

Our results suggest that climate warming will make O_3 pollution control more challengeable via altering clouds and SSRD and weakening the CRI. The high-level O_3 is not only influenced by changes in clouds and solar radiation related with short-term synoptic-scale circulation adjustments, but also modulated by long-term climate change. The occurrence likelihood of heatwaves (Chen et al., 2019; Ma et al., 2023), accompanied by fewer clouds and more SSRD, will increase under climate warming. Furthermore, if anthropogenic emissions are not greatly reduced, human-induced forcing will further amplify the probability (Faranda et al., 2023; King et al., 2016; Lopez et al., 2018; Sun et al., 2017; Zhang et al., 2024). Inevitably, the co-occurrence

561   of extreme high temperature and O_3 concentration is likely to occur frequently, posing
562   a greater threat to human health, crops, and vegetation. Therefore, we would like to
563   propose that more proactive human actions are vital to offset the penalty of climate
564   change to these issues.
565

566 **References**

567 Binkowski, F. S.: Models-3 Community Multiscale Air Quality (CMAQ) model aerosol
568   component 1. Model description, J. Geophys. Res., 108(D6), 2981,
569   doi:10.1029/2001JD001409, 2003.

570 Byun, D. W. and Ching, J. K. S.: Science algorithms of the EPA models-3 Community
571   Multiscale Air Quality (CMAQ) modeling system, U.S. Environmental Protection
572   Agency, Washington, D.C., 1999.

573 Chen, F. and Dudhia, J.: Coupling an Advanced Land Surface–Hydrology Model with
574   the Penn State–NCAR MM5 Modeling System. Part I: Model Implementation and
575   Sensitivity, Mon. Weather Rev., 129(4), 569–585, doi:10.1175/1520-
576   0493(2001)129<0569:CAALSH>2.0.CO;2, 2001.

577 Chen, R., Wen, Z., Lu, R. and Wang, C.: Causes of the Extreme Hot Midsummer in
578   Central and South China during 2017: Role of the Western Tropical Pacific
579   Warming, Adv. in Atmos. Sci., 36(5), 465–478, doi:10.1007/s00376-018-8177-4,
580   2019.

581 Creilson, J. K., Fishman, J. and Wozniak, A. E.: Arctic Oscillation-induced variability
582   in satellite-derived tropospheric ozone, Geophys. Res. Lett., 32(1), L14822,
583   doi:10.1029/2005GL023016, 2005.

584 Dong, Y., Li, J., Guo, J., Jiang, Z., Chu, Y., Chang, L., Yang, Y. and Liao, H.: The
585   impact of synoptic patterns on summertime ozone pollution in the North China Plain,
586   Science of The Total Environment, 735(C), 139559,
587   doi:10.1016/j.scitotenv.2020.139559, 2020.

588 Dudhia, J.: Numerical Study of Convection Observed during the Winter Monsoon
589   Experiment Using a Mesoscale Two-Dimensional Model, J. Atmos. Sci., 46(20),
590   3077–3107, doi:10.1175/1520-0469(1989)046<3077:NSOCOD>2.0.CO;2, 1989.

591 Faranda, D., Messori, G., Jezequel, A., Vrac, M. and Yiou, P.: Atmospheric circulation
592   compounds anthropogenic warming and impacts of climate extremes in Europe,
593   Proc Natl Acad Sci U S A, 120(13), e2214525120, doi:10.1073/pnas.2214525120,
594   2023.

595 Flynn, J., Lefer, B., Rappenglück, B., Leuchner, M., Perna, R., Dibb, J., Ziemba, L.,
596   Anderson, C., Stutz, J., Brune, W., Ren, X., Mao, J., Luke, W., Olson, J., Chen, G.
597   and Crawford, J.: Impact of clouds and aerosols on ozone production in Southeast
598   Texas, Atmos. Environ., 44(33), 4126–4133, 2010.

599 Fu, Y., Liao, H. and Yang, Y.: Interannual and Decadal Changes in Tropospheric Ozone
600   in China and the Associated Chemistry-Climate Interactions: A Review, Adv. in
601   Atmos. Sci., 36(9), 975–993, doi:10.1007/s00376-019-8216-9, 2019.

602 Gao, M., Wang, F., Ding, Y., Wu, Z., Xu, Y., Lu, X., Wang, Z., Carmichael, G. R. and
603   McElroy, M. B.: Large-scale climate patterns offer preseasonal hints on the co-
604   occurrence of heat wave and O3 pollution in China, Proc Natl Acad Sci U S A,
605   120(26), e2218274120, doi:10.1073/pnas.2218274120, 2023.

Grell, G. A., Peckham, S. E., Schmitz, R., McKeen, S. A., Frost, G., Skamarock, W. C. and Eder, B.: Fully coupled "online" chemistry within the WRF model, Atmos. Environ., 39(37), 6957–6975, doi:10.1016/j.atmosenv.2005.04.027, 2005.

Guenther, A., Karl, T., Harley, P., Wiedinmyer, C., Palmer, P. I. and Geron, C.: Estimates of global terrestrial isoprene emissions using MEGAN (Model of Emissions of Gases and Aerosols from Nature), Atmos. Chem. Phys., 6(11), 3181–3210, doi:10.5194/acp-6-3181-2006, 2006.

Hong, C., Zhang, Q., Zhang, Y., Davis, S. J., Tong, D., Zheng, Y., Liu, Z., Guan, D., He, K. and Schellnhuber, H. J.: Impacts of climate change on future air quality and human health in China, P. Natl. Acad. Sci. USA, 116(35), 17193–17200, doi:10.1073/pnas.1812881116, 2019.

Hong, S.-Y. and Lim, J.-O. J.: The WRF Single-Moment 6-Class Microphysical Scheme (WSM6), Journal of the Korean Meteorological Society, 42(2), 129–151, 2006.

Janjić, Z. I.: Nonsingular implementation of the Mellor-Yamada level 2.5 scheme in the NCEP meso model, Camp Springs, MD. 2002.

Ji, X., Chen, G., Chen, J., Xu, L., Lin, Z., Zhang, K., Fan, X., Li, M., Zhang, F., Wang, H., Huang, Z. and Hong, Y.: Meteorological impacts on the unexpected ozone pollution in coastal cities of China during the unprecedented hot summer of 2022, Science of The Total Environment, 914, 170035, doi:10.1016/j.scitotenv.2024.170035, 2024.

Jiang, Y., Wang, S., Xing, J., Zhao, B., Li, S., Chang, X., Zhang, S. and Dong, Z.: Ambient fine particulate matter and ozone pollution in China: synergy in anthropogenic emissions and atmospheric processes, Environ. Res. Lett., 1–21, doi:10.1088/1748-9326/aca16a, 2022.

Jiang, Z., Li, J., Lu, X., Gong, C., Zhang, L. and Liao, H.: Impact of western Pacific subtropical high on ozone pollution over eastern China, Atmos. Chem. Phys., 21(4), 2601–2613, doi:10.5194/acp-21-2601-2021, 2021.

Kang, H., Choi, Y.-S., Hwang, J. and Kim, H.-S.: On the cloud radiative effect for tropical high clouds overlying low clouds, Geoscience Letters, 1–6, doi:10.1186/s40562-020-00156-6, 2020.

King, A. D., Black, M. T., Min, S.-K., Fischer, E. M., Mitchell, D. M., Harrington, L. J. and Perkins-Kirkpatrick, S. E.: Emergence of heat extremes attributable to anthropogenic influences, Geophys. Res. Lett., 43(7), 3438–3443, doi:10.1002/2015GL067448, 2016.

Li, G., Bei, N., Cao, J., Huang, R., Wu, J., Feng, T., Wang, Y., Liu, S., Zhang, Q., Tie, X. and Molina, L. T.: A possible pathway for rapid growth of sulfate during haze days in China, Atmos. Chem. Phys., 17(5), 3301–3316, doi:10.5194/acp-17-3301-2017, 2017a.

Li, G., Bei, N., Tie, X. and Molina, L. T.: Aerosol effects on the photochemistry in

Mexico City during MCMA-2006/MILAGRO campaign, Atmos. Chem. Phys., 11(11), 5169–5182, doi:10.5194/acp-11-5169-2011, 2011a.

Li, G., Lei, W., Zavala, M., Volkamer, R., Dusanter, S., Stevens, P. and Molina, L. T.: Impacts of HONO sources on the photochemistry in Mexico City during the MCMA-2006/MILAGO Campaign, Atmos. Chem. Phys., 10(14), 6551–6567, doi:10.5194/acp-10-6551-2010, 2010.

Li, G., Zavala, M., Lei, W., Tsimpidi, A. P., Karydis, V. A., Pandis, S. N., Canagaratna, M. R. and Molina, L. T.: Simulations of organic aerosol concentrations in Mexico City using the WRF-CHEM model during the MCMA-2006/MILAGRO campaign, Atmos. Chem. Phys., 11(8), 3789–3809, doi:10.5194/acp-11-3789-2011, 2011b.

Li, H., Zheng, B., Lei, Y., Hauglustaine, D., Chen, C., Lin, X., Zhang, Y., Zhang, Q. and He, K.: Trends and drivers of anthropogenic NOx emissions in China since 2020, Environmental Science and Ecotechnology, 21, 100425, doi:10.1016/j.ese.2024.100425, 2024.

Li, K., Jacob, D. J., Liao, H., Shen, L., Zhang, Q. and Bates, K. H.: Anthropogenic drivers of 2013–2017 trends in summer surface ozone in China, vol. 116, pp. 422–427. 2019a.

Li, K., Jacob, D. J., Shen, L., Lu, X., De Smedt, I. and Liao, H.: Increases in surface ozone pollution in China from 2013 to 2019: anthropogenic and meteorological influences, Atmos. Chem. Phys., 20(19), 11423–11433, doi:10.5194/acp-20-11423-2020, 2020.

Li, L., An, J., Huang, L., Yan, R., Huang, C. and Yarwood, G.: Ozone source apportionment over the Yangtze River Delta region, China: Investigation of regional transport, sectoral contributions and seasonal differences, Atmos. Environ., 202, 269–280, doi:10.1016/j.atmosenv.2019.01.028, 2019b.

Li, M., Zhang, Q., Kurokawa, J.-I., Woo, J.-H., He, K., Lu, Z., Ohara, T., Song, Y., Streets, D. G., Carmichael, G. R., Cheng, Y., Hong, C., Huo, H., Jiang, X., Kang, S., Liu, F., Su, H. and Zheng, B.: MIX: a mosaic Asian anthropogenic emission inventory under the international collaboration framework of the MICS-Asia and HTAP, Atmos. Chem. Phys., 17(2), 935–963, doi:10.5194/acp-17-935-2017, 2017b.

Li, S., Wang, T., Huang, X., Pu, X., Li, M., Chen, P., Yang, X.-Q. and Wang, M.: Impact of East Asian Summer Monsoon on Surface Ozone Pattern in China, J. Geophys. Res., 123(2), 1401–1411, doi:10.1002/2017JD027190, 2018.

Liu, Y. and Wang, T.: Worsening urban ozone pollution in China from 2013 to 2017 - Part 1: The complex and varying roles of meteorology, Atmos. Chem. Phys., 20(1), 6305–6321, doi:10.5194/acp-20-6305-2020, 2020a.

Liu, Y., Geng, G., Cheng, J., Liu, Y., Xiao, Q., Liu, L., Shi, Q., Tong, D., He, K. and Zhang, Q.: Drivers of Increasing Ozone during the Two Phases of Clean Air Actions in China 2013-2020, Environmental Science & Technology, 57(24), 8954–8964, doi:10.1021/acs.est.3c00054, 2023.

686   Liu, Y. and Wang, T.: Worsening urban ozone pollution in China from 2013 to 2017 -
687   Part 2: The effects of emission changes and implications for multi-pollutant control,
688   Atmos. Chem. Phys., 20(1), 6323–6337, doi:10.5194/acp-20-6323-2020, 2020b.

689   Lopez, H., West, R., Dong, S., Goni, G., Ben Kirtman, Lee, S.-K. and Atlas, R.: Early
690   emergence of anthropogenically forced heat waves in the western United States and
691   Great Lakes, Nat. Clim. Change, 1–8, doi:10.1038/s41558-018-0116-y, 2018.

692   Lu, X., Zhang, L. and Shen, L.: Meteorology and Climate Influences on Tropospheric
693   Ozone: a Review of Natural Sources, Chemistry, and Transport Patterns, 1–23,
694   doi:10.1007/s40726-019-00118-3, 2019a.

695   Lu, X., Zhang, L., Chen, Y., Zhou, M., Zheng, B., Li, K., Liu, Y., Lin, J., Fu, T.-M. and
696   Zhang, Q.: Exploring 2016-2017 surface ozone pollution over China: source
697   contributions and meteorological influences, Atmos. Chem. Phys., 19(1), 8339–
698   8361, doi:10.5194/acp-19-8339-2019, 2019b.

699   Ma, Y.-Y., Chen, Y.-T., Hu, X.-X., Ma, Q.-R., Feng, T.-C., Feng, G.-L. and Di Ma:
700   The 2022 record-breaking high temperature in China: Sub-seasonal stepwise
701   enhanced characteristics, possible causes and its predictability, Advances in Climate
702   Change Research, 14(5), 651–659, doi:10.1016/j.accre.2023.09.008, 2023.

703   Mao, J., Wang, L., Lu, C., Liu, J., Li, M., Tang, G., Ji, D., Zhang, N. and Wang, Y.:
704   Meteorological mechanism for a large-scale persistent severe ozone pollution event
705   over eastern China in 2017, Journal of Environmental Sciences, 92, 187–199,
706   doi:10.1016/j.jes.2020.02.019, 2020.

707   Meehl, G. A., Tebaldi, C., Tilmes, S., Lamarque, J.-F., Bates, S., Pendergrass, A. and
708   Lombardozzi, D.: Future heat waves and surface ozone, Environ. Res. Lett., 13(6),
709   064004, doi:10.1088/1748-9326/aabcdc, 2018.

710   Mousavinezhad, S., Choi, Y., Pouyaei, A., Ghahremanloo, M. and Nelson, D. L.: A
711   comprehensive investigation of surface ozone pollution in China, 2015-2019:
712   Separating the contributions from meteorology and precursor emissions,
713   Atmospheric Research, 257, 105599, doi:10.1016/j.atmosres.2021.105599, 2021.

714   Nenes, A., Pandis, S. N. and Pilinis, C.: ISORROPIA: A new thermodynamic
715   equilibrium model for multiphase multicomponent inorganic aerosols, Aquatic
716   Geochemistry, 4(1), 123–152, doi:10.1023/A:1009604003981, 1998.

717   Pour-Biazar, A., McNider, R., Roselle, S., Suggs, R., Jedlovec, G., Byun, D., Kim, S.,
718   Lin, C., Ho, T., Haines, S., Dornblaser, B., Cameron, R.: Correcting photolysis rates
719   on the basis of satellite observed clouds, J. Geophys. Res., 112, D10302,
720   doi:10.1029/2006JD007422, 2007.

721   Pu, X., Wang, T. J., Huang, X., Melas, D., Zanis, P., Papanastasiou, D. K. and Poupkou,
722   A.: Enhanced surface ozone during the heat wave of 2013 in Yangtze River Delta
723   region, China, Science of The Total Environment, 603-604(C), 807–816,
724   doi:10.1016/j.scitotenv.2017.03.056, 2017.

725   Riahi, K., van Vuuren, D. P., Kriegler, E., Edmonds, J., O'Neill, B. C., Fujimori, S.,

Bauer, N., Calvin, K., Dellink, R., Fricko, O., Lutz, W., Popp, A., Cuaresma, J. C., KC, S., Leimbach, M., Jiang, L., Kram, T., Rao, S., Emmerling, J., Ebi, K., Hasegawa, T., Havlik, P., Humpenöder, F., Da Silva, L. A., Smith, S., Stehfest, E., Bosetti, V., Eom, J., Gernaat, D., Masui, T., Rogelj, J., Strefler, J., Drouet, L., Krey, V., Luderer, G., Harmsen, M., Takahashi, K., Baumstark, L., Doelman, J. C., Kainuma, M., Klimont, Z., Marangoni, G., Lotze-Campen, H., Obersteiner, M., Tabeau, A. and Tavoni, M.: The Shared Socioeconomic Pathways and their energy, land use, and greenhouse gas emissions implications: An overview, Global Environmental Change, 42, 153–168, doi:10.1016/j.gloenvcha.2016.05.009, 2017.

Shen, L. and Mickley, L. J.: Effects of El Niño on Summertime Ozone Air Quality in the Eastern United States, Geophys. Res. Lett., 44(2), 12–, doi:10.1002/2017GL076150, 2017.

Shu, L., Xie, M., Wang, T., Gao, D., Chen, P., Han, Y., Li, S., Zhuang, B. and Li, M.: Integrated studies of a regional ozone pollution synthetically affected by subtropical high and typhoon system in the Yangtze River Delta region, China, Atmos. Chem. Phys., 16(2), 15801–15819, doi:10.5194/acp-16-15801-2016, 2016.

Simayi, M., Shi, Y., Xi, Z., Ren, J., Hini, G. and Xie, S.: Emission trends of industrial VOCs in China since the clean air action and future reduction perspectives, Science of The Total Environment, 826(C), 153994, doi:10.1016/j.scitotenv.2022.153994, 2022.

Steiner, A. L., Davis, A. J., Sillman, S., Owen, R. C., Michalak, A. M. and Fiore, A. M.: Observed suppression of ozone formation at extremely high temperatures due to chemical and biophysical feedbacks, P. Natl. Acad. Sci. USA, 107, 19685–19690, doi:10.1073/pnas.1008336107, 2010.

Sun, Q., Miao, C., AghaKouchak, A. and Duan, Q.: Unraveling anthropogenic influence on the changing risk of heat waves in China, Geophys. Res. Lett., 44(1), 5078–5085, doi:10.1002/2017GL073531, 2017.

Tie, X., Long, X., Li, G., Zhao, S., Cao, J. and Xu, J.: Ozone enhancement due to the photodissociation of nitrous acid in eastern China, Atmos. Chem. Phys., 19(1), 11267–11278, doi:10.5194/acp-19-11267-2019, 2019.

Tie, X., Madronich, S., Walters, S., Zhang, R., Rasch, P. and Collins, W.: Effect of clouds on photolysis and oxidants in the troposphere, J. Geophys. Res., 108(D), 4642, doi:10.1029/2003JD003659, 2003.

Verstraeten, W. W., Neu, J. L., Williams, J. E., Bowman, K. W., Worden, J. R. and Boersma, K. F.: Rapid increases in tropospheric ozone production and export from China, Nature Geosci., 8(9), 690–695, doi:10.1038/ngeo2493, 2015.

Wang, L., Yang, X., Dong, J., Yang, Y., Ma, P. and Zhao, W.: Evolution of surface ozone pollution pattern in eastern China and its relationship with different intensity heatwaves, Environmental Pollution, 338, 122725, doi:10.1016/j.envpol.2023.122725, 2023.

766 Wang, N., Lyu, X., Deng, X., Huang, X., Jiang, F. and Ding, A.: Aggravating O_3
767   pollution due to NOx emission control in eastern China, Science of The Total
768   Environment, 677(C), 732–744, doi:10.1016/j.scitotenv.2019.04.388, 2019a.

769 Wang, T., Dai, J., Lam, K. S., Nan Poon, C. and Brasseur, G. P.: Twenty-Five Years of
770   Lower Tropospheric Ozone Observations in Tropical East Asia: The Influence of
771   Emissions and Weather Patterns, Geophys. Res. Lett., 46(2), 11463–11470,
772   doi:10.1029/2019GL084459, 2019b.

773 Wang, T., Xue, L., Feng, Z., Dai, J., Zhang, Y. and Tan, Y.: Ground-level ozone
774   pollution in China: a synthesis of recent findings on influencing factors and impacts,
775   Environ. Res. Lett., 17(6), 063003, doi:10.1088/1748-9326/ac69fe, 2022a.

776 Wang, W., Parrish, D. D., Wang, S., Bao, F., Ni, R., Li, X., Yang, S., Wang, H., Cheng,
777   Y. and Su, H.: Long-term trend of ozone pollution in China during 2014-2020:
778   distinct seasonal and spatial characteristics and ozone sensitivity, Atmos. Chem.
779   Phys., 22(1), 8935–8949, doi:10.5194/acp-22-8935-2022, 2022b.

780 Wang, Y., Gao, W., Wang, S., Song, T., Gong, Z., Ji, D., Wang, L., Liu, Z., Tang, G.,
781   Huo, Y., Tian, S., Li, J., Li, M., Yang, Y., Chu, B., Petäjä, T., Kerminen, V.-M., He,
782   H., Hao, J., Kulmala, M., Wang, Y. and Zhang, Y.: Contrasting trends of PM2.5 and
783   surface-ozone concentrations in China from 2013 to 2017, National Science Review,
784   7(8), 1331–1339, doi:10.1093/nsr/nwaa032, 2020.

785 Wesely, M. L.: Parameterization of surface resistances to gaseous dry deposition in
786   regional-scale numerical models, Atmospheric Environment (1967), 23(6), 1293–
787   1304, doi:10.1016/0004-6981(89)90153-4, 1989.

788 Willmott, C. J..: On the validation of models, Physical geography, 2(2), 184–194,
789   doi.org/10.1080/02723646.1981.10642213, 1981.

790 Xia, Y., Hu, Y., Huang, Y., Bian, J., Zhao, C., Wei, J., Yan, Y., Xie, F. and Lin, J.:
791   Concurrent hot extremes and high ultraviolet radiation in summer over the Yangtze
792   Plain and their possible impact on surface ozone, Environ. Res. Lett., 17(6), 064001,
793   doi:10.1088/1748-9326/ac6c3c, 2022.

794 Xiao, X., Xu, Y., Zhang, X., Wang, F., Lu, X., Cai, Z., Brasseur, G. and Gao, M.:
795   Amplified Upward Trend of the Joint Occurrences of Heat and Ozone Extremes in
796   China over 2013-20, Bull. Amer. Meteor. Soc., 103(5), E1330–E1342,
797   doi:10.1175/BAMS-D-21-0222.1, 2022.

798 Xu, L., Yu, J.-Y., Schnell, J. L. and Prather, M. J.: The seasonality and geographic
799   dependence of ENSO impacts on U.S. surface ozone variability, Geophys. Res. Lett.,
800   44(7), 3420–3428, doi:10.1002/2017GL073044, 2017.

801 Xue, L. K., Wang, T., Gao, J., Ding, A. J., Zhou, X. H., Blake, D. R., Wang, X. F.,
802   Saunders, S. M., Fan, S. J., Zuo, H. C., Zhang, Q. Z. and Wang, W. X.: Ground-level
803   ozone in four Chinese cities: precursors, regional transport and heterogeneous
804   processes, Atmos. Chem. Phys., 14(2), 13175–13188, doi:10.5194/acp-14-13175-
805   2014, 2014.

Yang, H., Chen, L., Liao, H., Zhu, J., Wang, W. and Li, X.: Impacts of aerosol–photolysis interaction and aerosol–radiation feedback on surface-layer ozone in North China during multi-pollutant air pollution episodes, Atmos. Chem. Phys., 22(6), 4101–4116, doi:10.5194/acp-22-4101-2022, 2022.

Yin, Z., Cao, B. and Wang, H.: Dominant patterns of summer ozone pollution in eastern China and associated atmospheric circulations, Atmos. Chem. Phys., 19(22), 13933–13943, doi:10.5194/acp-19-13933-2019, 2019.

Zeng, P., Lyu, X. P., Guo, H., Cheng, H. R., Jiang, F., Pan, W. Z., Wang, Z. W., Liang, S. W. and Hu, Y. Q.: Causes of ozone pollution in summer in Wuhan, Central China, Environmental Pollution, 241, 852–861, doi:10.1016/j.envpol.2018.05.042, 2018.

Zhang, L., Zhou, T., Zhang, X., Zhang, W., Li, L. and Li, L.: Attribution of the Extreme 2022 Summer Drought along the Yangtze River Valley in China Based on Detection and Attribution System of Chinese Academy of Sciences, Bull. Amer. Meteor. Soc., 1–6, doi:10.1175/BAMS-D-23-0258.1, 2024.

Zhang, Q., Zheng, Y., Tong, D., Shao, M., Wang, S., Zhang, Y., Xu, X., Wang, J., He, H., Liu, W., Ding, Y., Lei, Y., Li, J., Wang, Z., Zhang, X., Wang, Y., Cheng, J., Liu, Y., Shi, Q., Yan, L., Geng, G., Hong, C., Li, M., Liu, F., Zheng, B., Cao, J., Ding, A., Gao, J., Fu, Q., Huo, J., Liu, B., Liu, Z., Yang, F., He, K. and Hao, J.: Drivers of improved $PM_{2.5}$ air quality in China from 2013 to 2017, P. Natl. Acad. Sci. USA, 116(49), 24463–24469, doi:10.1073/pnas.1907956116, 2019.

Zhang, Y. and Zheng, J.: Blue Book on Ozone Pollution Prevention and Control in China (2020) [in Chinese], edited by Li, M., Science Press, Beijing, China, 121 pp., ISBN 9787030716644, 2022.

Zhao, C., Wang, Y., Yang, Q., Fu, R., Cunnold, D. and Choi, Y.: Impact of East Asian summer monsoon on the air quality over China: View from space, J. Geophys. Res., 115(D), D09301, doi:10.1029/2009JD012745, 2010.

Zhao, Z. and Wang, Y.: Influence of the West Pacific subtropical high on surface ozone daily variability in summertime over eastern China, Atmos. Environ., 170, 197–204, doi:10.1016/j.atmosenv.2017.09.024, 2017.

Zheng, B., Tong, D., Li, M., Liu, F., Hong, C., Geng, G., Li, H., Li, X., Peng, L., Qi, J., Yan, L., Zhang, Y., Zhao, H., Zheng, Y., He, K. and Zhang, Q.: Trends in China's anthropogenic emissions since 2010 as the consequence of clean air actions, Atmos. Chem. Phys., 18(1), 14095–14111, doi:10.5194/acp-18-14095-2018, 2018.

Zheng, H., Kong, S., He, Y., Song, C., Cheng, Y., Yao, L., Chen, N. and Zhu, B.: Enhanced ozone pollution in the summer of 2022 in China: The roles of meteorology and emission variations, Atmos. Environ., 301, 119701, doi:10.1016/j.atmosenv.2023.119701, 2023.

Zhou, D., Ding, A., Mao, H., Fu, C., Wang, T., Chan, L. Y., Ding, K., Zhang, Y., Liu, J., Lu, A. and Hao, N.: Impacts of the East Asian monsoon on lower tropospheric ozone over coastal South China, Environ. Res. Lett., 8(4), 044011,

846   doi:10.1088/1748-9326/8/4/044011, 2013.

847

848 **Data availability:**

849 Hourly observation data on mass concentrations of ambient air pollutants at surface

850 released by the Ministry of Ecology and Environment, China are available on the

851 website of *https://www.aqistudy.cn*.

852 Monthly mean low cloud cover and downward solar radiation from European Centre

853 for Medium-Range Weather Forecasts ERA5 reanalysis data are obtained by a

854 registration on the website of *https://cds.climate.copernicus.eu/datasets/reanalysis-*

855 *era5-single-levels-monthly-means?tab=download*.

856 Hourly observation data on meteorological parameters at weather stations are from

857 National Oceanic and Atmospheric Administration, available on the website of

858 *https://www.ncei.noaa.gov/maps/hourly*.

859 National Centers for Environmental Prediction Final Analyses data are from

860 *http://rda.ucar.edu/datasets/ds083.2*.

861 Initial and boundary chemical fields are available on the website of

862 *https://www.acom.ucar.edu/cam-chem/cam-chem.shtml*.

863 The MEIC emission inventory developed by Tsinghua University is from the website

864 of *http://meicmodel.org.cn*.

865 The projected total cloud cover percentage and surface downwelling shortwave

866 radiation are from *https://cds.climate.copernicus.eu/datasets/projections-*

867 *cmip6?tab=download*.

868

869 **Author contribution:** S.Z. and T.F. designed the research and analyze the results. T.F.

870 performed simulations, and S.Z. wrote the manuscript. X.T. provided useful comments

871 and suggestions on the structure and highlights of the paper. T.F. and M.D. revised the

872 manuscript. B.T., X.H., B.H., D.Y., and S.G. participated in data analysis and

873 discussions on the results.

874

875 **Competing interests:** The authors declare that they have no conflict of interest.

876

877 **Acknowledgements:** We would like to acknowledge China National Environmental

878 Monitoring Center, European Centre for Medium-Range Weather Forecasts, National

879 Oceanic and Atmospheric Administration, National Centers for Environmental

880 Prediction, and Tsinghua University for the free data availability. We also thank

881 anonymous reviewers for their insightful comments and suggestions.

882

883 **Financial support:** The research is supported by the National Natural Science

884 Foundation of China (42371093 and 42371080), Natural Science Foundation of Ningbo

885   Municipality (2023J208 and 2023J235), and Natural Science Foundation of Shaanxi

886   Province (2017JM4023).

887

888 **Figures and Tables**

889 **Table 1** Setup of model experiments.

Experiment	Anthropogenic emission	Meteorology	Cloud-radiation interactions (CRI)
BS Exp._CRI	Emission 2022	Meteorology 2022	Yes
BS Exp._noCRI	Emission 2022	Meteorology 2022	No
CTRL Exp.1_CRI	Emission 2022	Meteorology 2021	Yes
CTRL Exp.1_noCRI	Emission 2022	Meteorology 2021	No
CTRL Exp.2	Emission 2021	Meteorology 2022	Yes
BG Exp.	No	Meteorology 2022	Yes

890

891
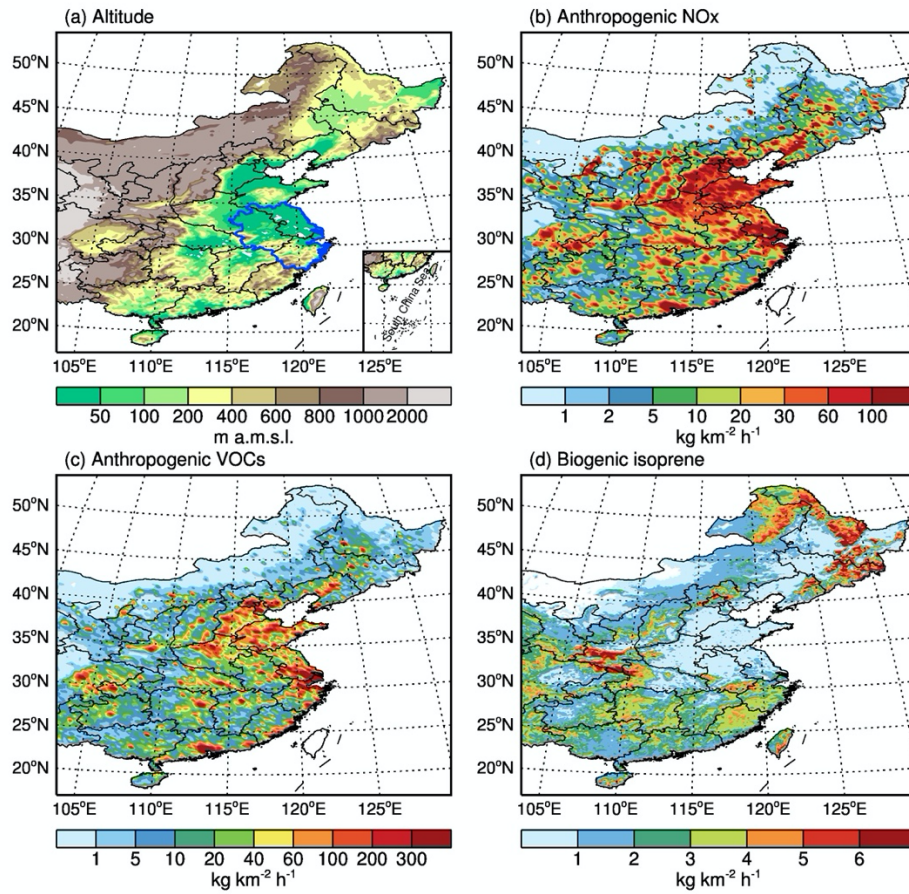
892
Figure 1 Location of the YRD, China and spatial distributions of emissions. (a) The
flat YRD is located in the eastern China, marked by the blue line. (b) Anthropogenic
NO_x emission rate in July 2022 based on the MEIC emission inventory. (c) Same as (b),
but for anthropogenic non-methane VOCs. (b) and (c) represent human-induced
emissions of precursors for O_3. (d) Biogenic isoprene emission rate is calculated by
MAGAN, representing biogenic VOCs emissions.

899

900

901
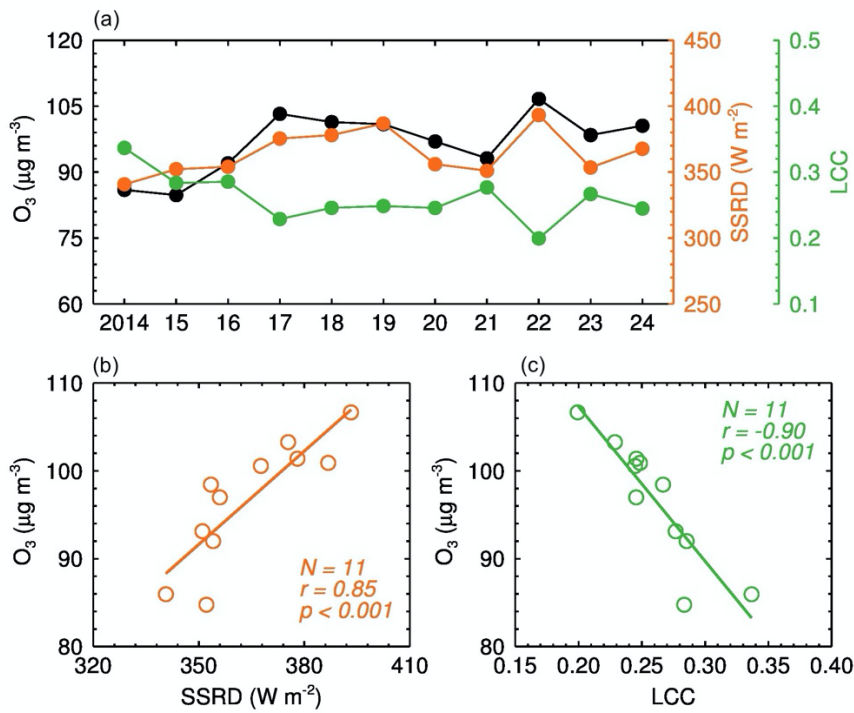
Figure 2 Observed relationships between O_3, SSRD, and LCC. (a) Annual variation in mean daytime O_3 concentration (black), SSRD (orange), and LCC (green) during the warm season of the past decade (2014-2024) in the YRD, China. (b) Correlation between O_3 concentration and SSRD. (c) Correlation between O_3 concentration and LCC. The colored lines in (b) and (c) represent the linear fits through the data in (a), i.e., $[O_3] = -32.20 + 0.35 \times [SSRD]$ with $r = 0.85$ and $[O_3] = 142.49 - 173.87 \times [LCC]$ with $r = -0.90$. O_3 concentration is significantly positively (negatively) correlated with SSRD (LCC), with confidence levels exceeding 99.9%. Sample sizes N, correlation coefficients r, and confidence levels p by the Student's t-test are shown in (b) and (c).

911

912
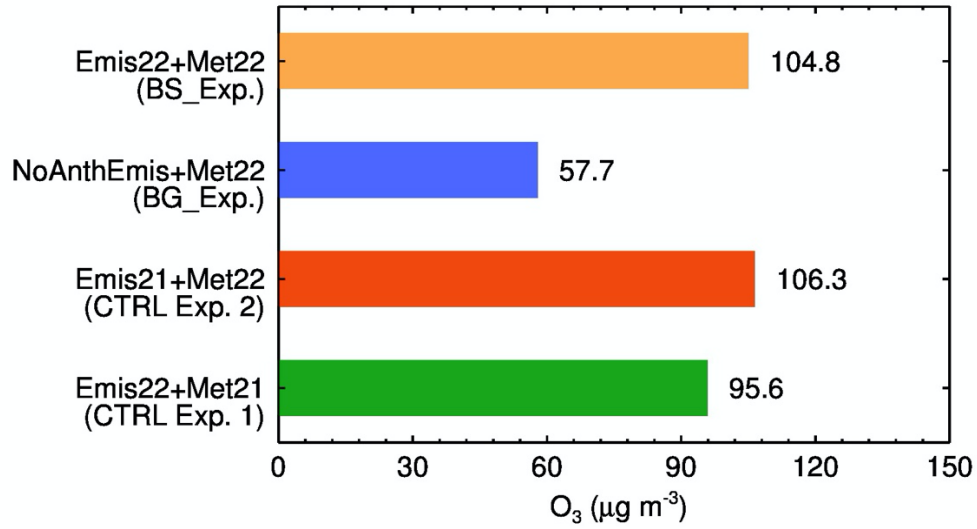
913 **Figure 3** Simulated O_3 concentrations under different model experiments.
914 Contributions of background input (blue) and anthropogenic emissions (orange *minus*
915 blue) to summer O_3 concentrations in the YRD. Contributions of emission change
916 (orange *minus* red) and meteorology change (orange *minus* green) to O_3 change.

917

918

919
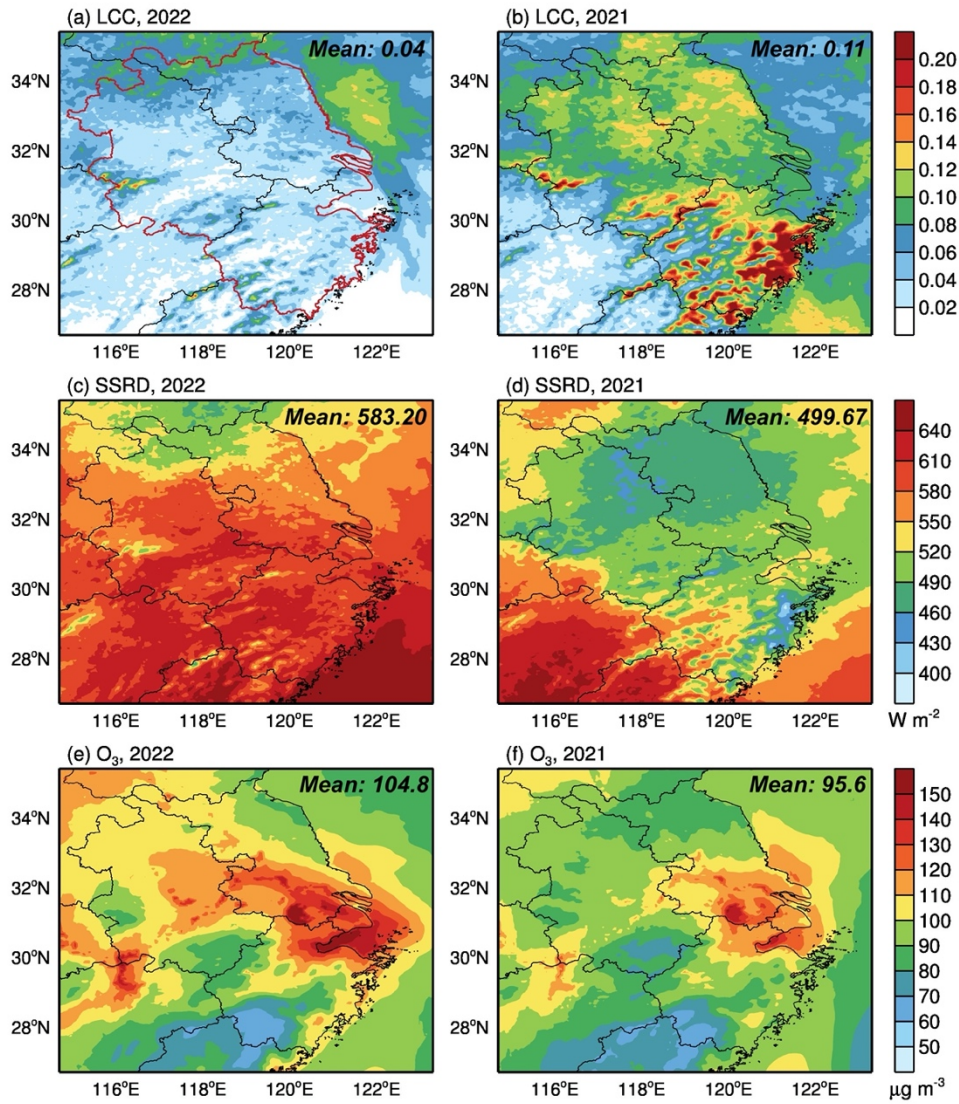
920 **Figure 4** Comparison of spatial distribution of monthly mean daytime O₃
921 concentrations under different CRI intensities. (a-b) LCC in July 2022 and July 2021,
922 respectively. (c-d) SSRD. (e-f) Daytime O₃ concentrations. (a) and (c) represent a weak
923 CRI mechanism due to less LCC and more SSRD, corresponding to higher O₃
924 concentrations, with a larger spatial coverage. (b) and (d) represent a strong CRI
925 mechanism due to more LCC and less SSRD, corresponding to lower O₃ concentrations,
926 with a smaller spatial coverage. The YRD is enclosed by the red line in (a). The regional
927 average of each variable is shown at the top-right corner of each panel.

928

929

930
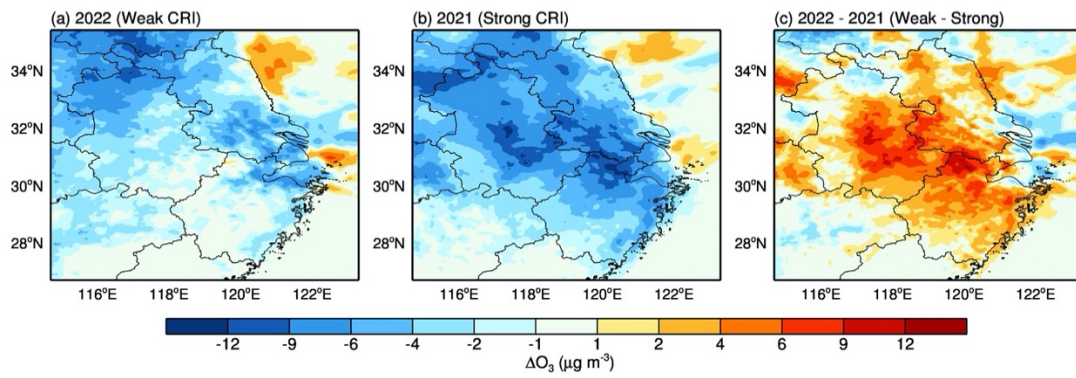
931 **Figure 5** Influence of CRI on O_3 change. (a) Difference in O_3 concentrations including
932 and excluding CRI in July 2022, indicating O_3 change caused by a weak CRI. (b) Same
933 as (a) but in July 2021, indicating O_3 change caused by a strong CRI. (c) A result of (a)
934 *minus* (b), representing ΔO_3 change caused by the CRI intensity change.
935

936

937
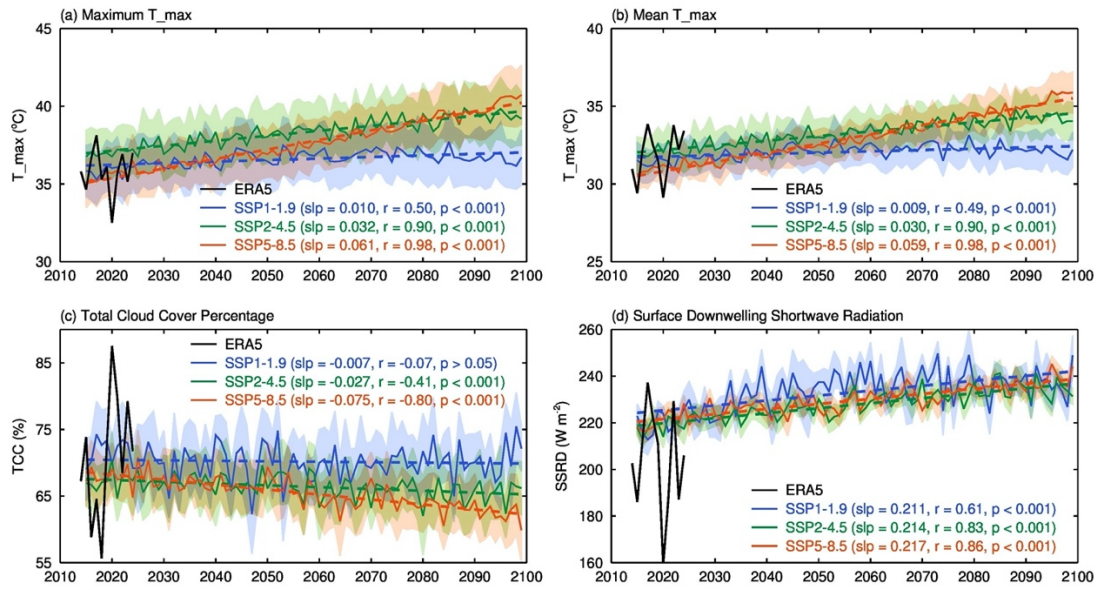
Figure 6 Trends of multi-model ensemble mean radiation conditions projected by the CMIP6 under three SSPs during 2015-2099. (a) The maximum daily T_max, and (b) The mean daily T_max in July, represent the extreme and mean status of high temperature, respectively. (c) TCC and (d) SSRD together reflect the solar radiation conditions for O_3 formation. The shading shows ±1.0 standard error, and the dash lines represent the linear trends of each variable under different SSPs. The black curve in each panel shows the real variation of each variable from the ERA5 reanalysis data during 2014-2024.